

# Use of dynamic reconstruction for parametric Patlak imaging in dynamic whole body PET

Zacharias Chalampalak<sup>1</sup>, Simon Stute<sup>2,3</sup>, Marina Filipović<sup>1</sup>,  
Florent Sureau<sup>1</sup> and Claude Comtat<sup>1</sup>

<sup>1</sup>Laboratoire d’Imagerie Biomédicale Multimodale (BioMaps), Université Paris-Saclay, CEA, CNRS, Inserm, Service Hospitalier Frédéric Joliot, Orsay, France

<sup>2</sup>Nuclear Medicine Department, Nantes University Hospital, Nantes, France.

<sup>3</sup> CRCINA, Inserm, CNRS, Université d’Angers, Université de Nantes, France

E-mail: zacharias.chalampalakis@outlook.com

**Keywords:** Dynamic reconstruction, 4D reconstruction, Spectral model, Patlak model, Dynamic whole body PET, Parametric imaging

May 2021

**Abstract.** Dynamic Whole Body (DWB) PET acquisition protocols enable the use of whole body parametric imaging for clinical applications. In FDG imaging, accurate parametric images of Patlak  $K_i$  can be complementary to standard SUV images and improve on current applications or enable new ones. In this study we consider DWB protocols implemented on clinical scanners with limited axial field of view with use of multiple whole body sweeps. These protocols result in temporal gaps in the dynamic data which produce noisier and potentially more biased parametric images, compared to single bed dynamic protocols. Dynamic reconstruction using the Patlak model has been previously proposed to overcome these limits and shown improved DWB parametric images of  $K_i$ . In this work we propose and make use of a spectral analysis based model for DWB dynamic reconstruction and parametric imaging of Patlak  $K_i$ . Both dynamic reconstruction methods were evaluated and compared against 3D reconstruction based parametric imaging from single bed dynamic protocols. This work was conducted on simulated data and results were tested against a real FDG dynamic dataset. We showed that dynamic reconstruction can achieve levels of parametric image noise and bias comparable to 3D reconstruction in single bed dynamic studies, with the spectral analysis model offering additional flexibility and further reduction of image noise. Comparisons were also made between step and shoot and Continuous Bed Motion (CBM) protocols, which showed that CBM can achieve lower parametric image noise due to reduced acquisition temporal gaps. Finally, our results showed that dynamic reconstruction improved VOI parametric mean estimates but did not result to fully converged values before resulting in undesirable levels of noise. Additional regularisation methods need to be considered for DWB protocols to ensure both accurate quantification and acceptable noise levels for clinical applications.

## 1. Introduction

Positron Emission Tomography (PET) imaging is well known and established in clinical applications and pathways, with an important role towards the delivery of precision medicine (Subramaniam 2017). The established clinical practices rely on static imaging after a certain uptake period and semi-quantitative measures, such as the standardised uptake value (SUV). But these measures are vulnerable to many unknown factors that can vary between PET examinations, such as body composition, retention clearance, inconsistencies in uptake time and imaging practices (Boellaard 2011). On the other hand dynamic PET imaging can be used to fully characterise underlying tracer kinetics and provide fully quantitative measures, that could overcome many limitations of current static imaging practices and enable use of PET for new applications in clinical practice (Lammertsma 2017, Dimitrakopoulou-Strauss et al. 2021, Meikle et al. 2021). Current clinical scanners are limited in coverage by their axial field of view (A-FOV), with values ranging from 15 to 26 cm (Vandenberghe et al. 2020). This is sufficient for single organ dynamic studies but cannot directly provide synchronous whole-body coverage, which is essential for some clinical applications such as tumour staging in oncology. In practice for static imaging whole-body coverage is achieved using multiple bed positions at different axial locations to provide the desired axial coverage (Schubert et al. 1996), or alternatively via continuous axial bed motion (CBM) during the acquisition (Panin et al. 2014). Recently scanners with increased A-FOV have been developed (Karp et al. 2020, Siegel et al. 2020), even with nearly 2 meters long A-FOV which provides total-body coverage (Cherry et al. 2018). But these scanners are still not widely adopted in the clinic. Using similar methods as in static whole-body imaging, dynamic whole body (DWB) protocols have been developed using multiple bed positions and repeated whole-body passes (Karakatsanis et al. 2011, Karakatsanis et al. 2013, Rahmim et al. 2019). These types of acquisition protocols have also been incorporated into clinical products (Hu et al. 2020), and it has been shown that their use in clinical practice is feasible (Fahrni et al. 2019, Dias et al. 2020).

The immediate effect of transition from single bed dynamic studies to multi-bed dynamic studies is the introduction of temporal gaps in the acquired data of any given bed position. These are introduced at each bed position by the time spent on imaging other bed positions and by scanner system delays due to the time required to move the bed to the next position and prepare for the next acquisition. These gaps cause a significant reduction in the sensitivity of the acquisition, with fewer total counts collected for each axial location when compared to single bed dynamic acquisitions. Furthermore, estimation of fast temporal changes in tracer uptake are compromised as the early time points of the acquisition are not fully sampled for all beds. Finally the established clinical protocols that make use of image derived input function (IDIF) to ease integration in clinical practice further sacrifice imaging time in the study's early phase, which is spent in acquiring fast frames over a single bed location centred over the heart and the aorta (Hu et al. 2020).

The generation of parametric images from dynamic data requires fitting of the dynamic model of interest on time activity curves (TAC) for every voxel in the image. Due to the poor statistics and high noise associated with TAC measurements at the voxel level, in particular for DWB acquisitions, parametric image estimates can be heavily corrupted by noise and potentially biased. The use of direct dynamic reconstruction has been proposed to improve on this task by making use of dynamic models directly in the reconstruction. These techniques allow for more accurate modelling of the noise from the raw PET data in the generation process of parametric images and can improve parametric image noise and reduce bias (Reader & Verhaeghe 2014). For DWB acquisitions specifically, it has been shown using simulated and real data that direct dynamic reconstruction provides reduced noise, bias and improved parametric image contrast when compared to post-reconstruction parametric imaging (Karakatsanis, Casey, Lodge, Rahmim & Zaidi 2016).

In this work, we evaluate the performance of dynamic reconstruction algorithms for DWB fluorodeoxyglucose ( $[^{18}\text{F}]\text{FDG}$ ) PET imaging for various dynamic reconstruction methods and for different DWB acquisition protocols. The evaluation is based on simulations of single bed and multi-bed dynamic studies and results are illustrated in a real dynamic FDG PET study.

In detail we evaluate for WB Patlak  $K_i$  parametric imaging (1) the benefits of using direct Patlak dynamic reconstruction in DWB protocols against single bed dynamic protocols and indirect parametric imaging from regular 3D reconstruction, (2) the use of the Spectral analysis dynamic model (Cunningham & Jones 1993) in dynamic reconstruction for indirect parametric imaging, (3) the use of two different optimization algorithms for dynamic reconstruction and finally (4) the impact of different DWB acquisition strategies.

## 2. Methods

### 2.1. Simulated acquisition protocols

A single bed (SB) dynamic protocol (continuous in time with no temporal gaps) and three DWB acquisition protocols of five bed positions (with temporal gaps) were simulated for this study, using the geometry characteristics of the GE Signa PET/MR scanner (Grant et al. 2016). With the provided 25 cm A-FOV per bed and a bed overlap of 3.34 cm, axial coverage of 110.3 cm can be achieved with five bed positions. The relatively small overlap (approximately half compared to routine clinical protocols) was selected to reduce the number of beds and subsequently the acquisition temporal gaps. A total study duration of 60 minutes was used in the design of all protocols, including an initial single bed dynamic phase of 3 minutes centred over the aorta to mimic requirements for IDIF estimation.

- The first DWB protocol (DWB-1) considers a step and shoot (S&S) acquisition using the timing characteristics of the Signa PET/MR, with a delay of 6 seconds

between adjacent bed positions and 36 seconds between whole-body sweeps, resulting to 8 whole-body sweeps in the duration of the study.

- The second DWB protocol (DWB-2) differs from DWB-1 by use of system delays that mimic a continuous bed motion (CBM) acquisition of the same length, with no delays between adjacent bed positions and 12 seconds delay between whole-body sweeps to account for bed speed and acquisition overscan (used to obtain reasonable axial sensitivity at the edges of the acquisition (Panin et al. 2014)). This protocol results to 9 whole-body sweeps. The actual simulation for DWB-2 did not make use of continuous bed motion in the simulation process but made use of the accurate timings that reflect reduction of delays and framing achieved with CBM on the same system geometry. This is conceptually equivalent to CBM sinogram data (sometimes refereed as "chunks" (Hu et al. 2014)) with uniform framing over the FOV instead of slice-dependent timings as in actual CBM sinograms.
- The third DWB protocol (DWB-3) replicates the timing properties of DWB-2 for CBM acquisition but utilises a bi-directional acquisition that reduces delays between sweeps to the time spent for the over-scan. This acquisition motion provides more sweeps in the same study duration but results in non-uniform sampling. This protocol results to 10 whole-body sweeps.

Our study focuses on the second axial bed location for the DWB simulations, centred over the upper chest as seen in figure 1. The PET data simulations were conducted solely for this bed position using the framing of the protocols described above. The exact framing information are available in the supplementary material.

## 2.2. Digital phantom & analytical simulation

The Zubal brain phantom (Zubal et al. 1994) was chosen for the simulations of PET [ $^{18}\text{F}$ ]FDG data, even though its anatomy doesn't correspond to the anatomy that would be found in the axial location of the simulated bed position. The choice of the phantom was made to incorporate higher complexity structures than those offered from common lung/chest phantoms. Furthermore the use of the brain phantom, centred in the FOV, aided in avoiding analysis of areas falling in the overlapping regions, whose behaviour under DWB acquisition and reconstruction is yet another subject for investigation. The Zubal brain phantom was segmented into 19 unique regions and a non-reversible two tissue compartment model was assigned uniformly to each region to simulate realistic FDG kinetics, with  $K_1$ ,  $k_2$ ,  $k_3$  and  $V_b$  values drawn from the literature and a real measured input function. A selection of the simulated kinetic parameters is provided in the supplementary material. An analytical simulator was used to generate raw PET sinogram data (Stute et al. 2015). The simulations included attenuation and detector resolution effects, scattered and random coincidences, while Poisson noise was added to the sinogram data. The simulation did not include time of flight (TOF) information in

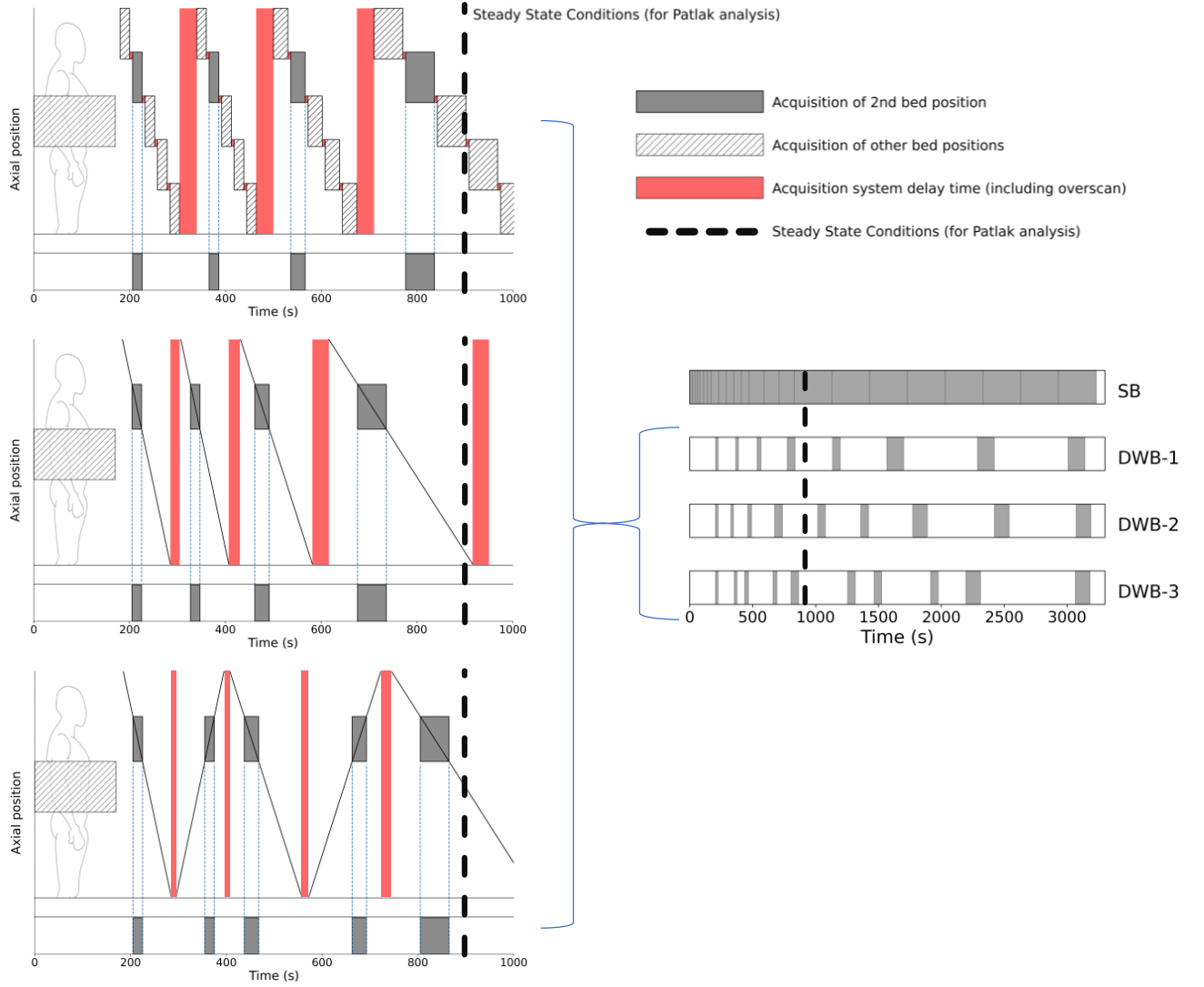


**Figure 1.** Dynamic whole-body acquisition protocols considered for simulation.

the data. Fifty different noise realisations were simulated for each DWB protocol. For the SB protocol the number of noise realisation was reduced to twenty as simulation and reconstruction times of the SB datasets were substantially higher.

### 2.3. Reconstruction and kinetic modelling

Both 3D and dynamic iterative reconstructions were used. All reconstructions were run within an OSEM framework, for 40 iterations and 28 subsets, using the open source fully quantitative reconstruction platform CASToR (Merlin et al. 2018). All reconstructions were performed with a voxel size of  $2.2 \text{ mm} \times 2.2 \text{ mm} \times 2.8 \text{ mm}$  and included resolution modeling as well as corrections for attenuation and for random and scattered coincidences (generated from the simulation). Dynamic reconstructions

are made by combining dynamic models that describe the tracer kinetics with the tomographic reconstruction process. When the dynamic model of interest is used this technique results in direct reconstruction of parametric images of interest and allows for accurate modeling of the raw data noise in the estimation process (Carson & Lange 1985, Matthews et al. 1995, Kamasak et al. 2005, Wang et al. 2008). Use of generic dynamic models can also be made for dynamic reconstruction, where dynamic models impose temporal regularisation in the frame activity estimation process. Post-reconstruction (indirect) estimation of parametric images can then be made and indirectly benefit from the use of dynamic reconstruction (Reader & Verhaeghe 2014, Novosad & Reader 2016). Linear dynamic models can be directly implemented within the system matrix (Matthews et al. 1995, Wang et al. 2008, Reader & Verhaeghe 2014) but result in algorithms with substantially slower overall convergence properties. Instead a nested optimization framework (Wang & Qi 2010, Matthews et al. 2010) can be used, which decouples the dynamic model fitting process on image space data from the tomographic update process over the raw PET data. This allows for multiple nested sub-iterations of dynamic model fitting to be run within each tomographic iteration of the reconstruction process, resulting in convergence acceleration and reasonable computing time requirements. The separation of the two processes allows for various optimization algorithms to be implemented in the nested dynamic model fitting process (Matthews et al. 2010). One particular method of interest is the Non-Negative Least Squares (NNLS) algorithm (Lawson & Hanson 1995), that enforces non-negativity and is commonly used in post-reconstruction kinetic modeling. The NNLS algorithm is self-terminating and for dynamic reconstruction it has been shown that a single execution of nested NNLS results to parametric images with similar Root Mean Square Error (RMSE) to that of 15 iterations of nested MLEM (Matthews et al. 2010). Therefore use of nested NNLS optimization has the potential for reduced overall reconstruction times. In this work we made use of both nested MLEM and NNLS optimizations to compare their performance and reconstruction time requirements for their implementation within CASToR. The nested MLEM optimization was used with 20 sub-iterations of the dynamic model fitting process after each subset of the OSEM tomographic update process, which has been found to be the optimal number of sub-iterations in a previous similar study (Karakatsanis, Casey, Lodge, Rahmim & Zaidi 2016). Hereafter we will refer to nested dynamic reconstruction simply as *4D reconstruction*.

In this work we evaluated two different linear dynamic models for 4D reconstructions, the Patlak model and the Spectral analysis model.

- 4D Patlak:

The Patlak model describes the activity in tissue  $C_T(t)$  as

$$C_T(t) = K_i \int_0^t C_P(\tau) d\tau + V_\alpha C_P(t) , \quad t > t_{ss} , \quad (1)$$

where  $C_P$  is the activity concentration in arterial blood plasma at time point  $t$ ,  $K_i$

is the steady state trapping rate and  $V_\alpha$  the apparent volume of distribution. The Patlak model is valid once steady state conditions have been reached (denoted as  $t_{ss}$ ). For a PET measurement the observed activity is

$$C_{PET}(t) = (1 - V_B)C_T(t) + V_B C_B(t), \quad (2)$$

where conventionally it is assumed that the blood fraction  $V_B$  is small ( $\leq 0.05$ ) in most tissues. If we assume for FDG that the total blood activity concentration  $C_B$  is proportional to  $C_P$  with  $C_B = rC_P$ , define the Patlak slope  $\theta_1 = (1 - V_B)K_i$  and the Patlak intercept  $\theta_2 = V_\alpha + rV_B$ , then the observed activity of acquisition frame  $f$  between time points  $t_{start}$  and  $t_{end}$  is modelled according to the Patlak model as

$$\int_{t_{start}}^{t_{end}} \mathbf{C}_{PET}(\tau) d\tau = \boldsymbol{\theta}_1 \int_{t_{start}}^{t_{end}} \int_0^\tau C_P(\tau_1) d\tau_1 d\tau + \boldsymbol{\theta}_2 \int_{t_{start}}^{t_{end}} C_P(\tau) d\tau, \quad (3)$$

where  $\mathbf{C}_{PET}(t)$  is the observed activity map. Using this representation a linear model of two basis functions can be constructed, which when fitted to TAC data provides parametric images  $\boldsymbol{\theta} = [\boldsymbol{\theta}_1, \boldsymbol{\theta}_2]$ . 4D dynamic reconstruction with the Patlak model directly results to parametric images of  $\boldsymbol{\theta}_1$  and  $\boldsymbol{\theta}_2$ . In our study 4D Patlak reconstruction was applied using frame data after the first 15 minutes, from where we assumed steady state conditions ( $t_{ss} = 15$  min).

It is important to note that a limitation of the Patlak model is that the estimated  $K_i$  from the Patlak slope  $\theta_1$  is susceptible to systematic errors in its estimation and can deviate from the true underlying  $K_i (= \frac{K_1 k_3}{k_2 + k_3})$ . In addition,  $V_B$  is not necessarily known a priori and Patlak analysis can not distinguish between  $K_i$  and  $(1 - V_B)$ . In this study we use the Patlak slope  $\theta_1$  as the  $K_i$  value of interest for parametric imaging, as well as the ground truth target, generated from Patlak fits on noiseless simulated TAC data.

- 4D Spectral: 4D reconstruction using the spectral analysis model is inspired from the 1993 homonym method (Cunningham & Jones 1993) that is used to describe the generic behaviour of any compartmental system as a sum of decaying exponential functions with decay rates  $\beta$  which describe the exchange between compartments, convolved with an input function (Gunn et al. 2002). For a measurement within an acquisition frame  $f$  between time points  $t_{start}$  and  $t_{end}$ , the observed PET activity can be described according to the Spectral analysis model with  $M+1$  number of parameters  $\phi$  as

$$\int_{t_{start}}^{t_{end}} \mathbf{C}_{PET}(\tau) d\tau = \sum_{b=0}^{M-1} \phi_b \int_{t_{start}}^{t_{end}} e^{-\beta_b \tau} * C_P(\tau) d\tau + \phi_M \int_{t_{start}}^{t_{end}} C_P(\tau) d\tau. \quad (4)$$

Assuming  $C_B$  is proportional to  $C_P$  then the parametric map  $\phi_M$  is proportional to the blood fraction  $V_B$ , while for irreversible kinetics the decay rate  $\beta_0 \rightarrow 0$

and the parametric map  $\phi_0$  describes tracer trapping. Parametric maps  $\phi_1 \dots \phi_{M-1}$  describe the exchange between compartments, with decay rates  $\beta_1 \dots \beta_{M-1}$  chosen to be logarithmic spaced within a range of values that covers the expected underlying kinetics. In our tests we used 3 different sets of numbers of basis functions ( $M+1=17, 9$  and  $6$ ), with  $\beta_1 \dots \beta_{M-1}$  logarithmically spaced within the range of 3 to  $0.001 \text{ min}^{-1}$ .

Unlike the Patlak model, the spectral analysis model is valid from the start of the acquisition and by default was applied to all time frames. The parameters  $\phi_b$  of the spectral model have physiological meaning and in combination can be used to derive macro-parameters maps such as  $K_1$  and either  $K_i$  or  $V_D$ , depending on the irreversible or reversible kinetic behaviour (Gunn et al. 2002). However, this derivation implies that the acquisition starts at the injection time, which is not the case for DWP protocols, except for the bed position corresponding to the initial dynamic phase used for IDIF estimation. In our study, the spectral analysis model is used to enforce temporal regularisation without any strong assumptions on an underlying model (Reader et al. 2007). The activity estimates of the 4D Spectral reconstruction are fitted post-reconstruction with the Patlak model to estimate the parametric images of Patlak  $K_i$ . In this sense the use of 4D Spectral reconstruction for parametric  $K_i$  imaging can be regarded as indirect dynamic reconstruction.

As highlighted above the spectral analysis model makes use of all frame data, while the Patlak model uses data after  $t_{ss}$ . In order to make a closer comparison between the two models for 4D reconstruction, an additional comparison was made using only data after  $t_{ss}$  (reconstructions labelled with  $t > t_{ss}$ ).

With the exception of 4D Patlak reconstructions that directly output parametric images of  $K_i$ , all other 4D and 3D reconstruction activity maps were fitted post-reconstruction with the Patlak model at the voxel level, using the Ordinary Least Squares (OLS) optimization algorithm, to generate parametric  $K_i$  images. For all 4D reconstructions and post-reconstruction fitting processes the true input function was used.

The reconstruction's namings and parameters are summarised in table1 and table 2.

#### 2.4. Evaluation metrics

The reconstructed and generated parametric  $K_i$  images were evaluated across noise realisations for voxel based and Volumes of Interest (VOI) based metrics. We define  $\theta_{j,n}$  as the image  $K_i$  value for voxel  $j$  in noise realisation  $n$ ,  $\theta_{VOI,n}$  the VOI  $K_i$  mean value and  $\theta_{VOI}^{GT}$  the ground truth value (as measured from Patlak analysis on the noiseless simulated TACs). The following voxel-based metrics were calculated, where (7) is the Root Mean Square (RMS) spatial average of (5) and (6) within a VOI.

$$Bias_j = \bar{\theta}_j - \theta_{VOI}^{GT} \quad , \text{ where } \bar{\theta}_j = \frac{1}{N_{noise}} \sum_{n=1}^{N_{noise}} \theta_{j,n} \quad (5)$$



**Table 1.** Evaluated reconstruction parameters.

Name	Dynamic model	Nested Optmization	Algorithm
3D	none	n/a	OSEM(40it28s)
4D Patlak	Patlak	MLEM (20sub-it)	OSEM(40it28s)
4D Spectral(6bf)	Spectral	MLEM (20sub-it)	OSEM(40it28s)
4D Spectral(9bf)	Spectral	MLEM (20sub-it)	OSEM(40it28s)
4D Spectral(17bf)	Spectral	MLEM (20sub-it)	OSEM(40it28s)
4D Spectral(6bf)-NNLS	Spectral	NNLS	OSEM(40it28s)
4D Spectral(9bf)-NNLS	Spectral	NNLS	OSEM(40it28s)
4D Spectral(17bf)-NNLS	Spectral	NNLS	OSEM(40it28s)

**Table 2.** Additional reconstructions characteristics.

Additional Reconstructions	Characteristics
4D Spectral(6bf) $t > t_{ss}$	Provided only with data after $t_{ss}$
4D Spectral(9bf) $t > t_{ss}$	Provided only with data after $t_{ss}$

$$CoV_j = \frac{1}{\theta_{VOI}^{GT}} \sqrt{\frac{1}{N_{noise}} \sum_{n=1}^{N_{noise}} (\theta_{j,n} - \bar{\theta}_j)^2} \quad (6)$$

$$\text{Metrics for } j \in VOI \left\{ \begin{array}{l} \%RMS \text{ Bias} : \frac{100}{\theta_{VOI}^{GT}} \sqrt{\frac{1}{N_{VOI}} \sum_{j \in VOI} Bias_j^2} \\ \%RMS \text{ CoV} : \sqrt{\frac{1}{N_{VOI}} \sum_{j \in VOI} CoV_j^2} \times 100 \end{array} \right. \quad (7)$$

The following metrics were used for VOI-based analysis, with the average VOI value being the parameter of interest (as opposed to the pixel value).

$$\text{Metrics for } VOI \left\{ \begin{array}{l} \%Bias_{\theta_{VOI}} = \frac{100}{\theta_{VOI}^{GT} N_{noise}} \sum_{n=1}^{N_{noise}} (\theta_{VOI,n} - \theta_{VOI}^{GT}) \\ \%CoV_{\theta_{VOI}} = \frac{100}{\theta_{VOI}^{GT}} \sqrt{\frac{1}{N_{noise}} \sum_{n=1}^{N_{noise}} (\theta_{VOI,n} - \bar{\theta}_{VOI})^2} \end{array} \right. \quad (8)$$

Because Patlak analysis provides different fits on the simulated TACs depending on the DWB protocol framing, the  $\theta_{VOI}^{GT}$  differ slightly per protocol. The ground truth values used in the evaluations are given in table 3. The cortex and an eroded thalamus VOI were evaluated in the analysis. The thalamus VOI was eroded by 2 voxels in order to be less susceptible to partial volume effects. By contrast the cortex VOI is subject to partial volume effects.

**Table 3.**  $\theta_{VOI}^{GT}$  and true  $K_i$  values for the simulated acquisition protocols ( $\text{min}^{-1}$ ).

VOI Name	SB	DWB-1	DWB-2	DWB-3	$K_i$
Thalamus	0.0305	0.0309	0.0311	0.0303	0.0307
Cortex	0.0390	0.0391	0.0392	0.0388	0.0410

### 2.5. Real Data

A single-bed dynamic examination centred over the lungs region was used to test performance of the evaluated algorithms and to compare results against the simulation findings. Approval for the retrospective use of the real patient data was obtained for this study. The data had been collected with approval from an local ethics committee. The original dataset was acquired on a Signa PET/MR, starting at the injection of 177 MBq of FDG tracer to the patient, for a duration of 1 hour. The imaged patient had been diagnosed with a non small cell lung cancer (NSCLC) at the left lung. The raw list-mode dataset was retrospectively reprocessed (replayed) to create two new datasets. One dataset using the framing of the simulated single bed (SB) study and one dataset using the framing of the simulated DWB-1 study (DWB) including temporal gaps. Both datasets included TOF information provided by the Signa PET-MR which was used in the reconstruction process. An IDIF from the ascending aorta was measured on activity image data from 3D reconstruction and used for 4D reconstruction and post-reconstruction analysis. The two datasets were reconstructed using the same 3D and 4D dynamic reconstruction algorithms that were used in the simulation study using identical parameters. No respiratory motion correction or gating was applied on the data. Similar to the simulation study, post reconstruction Patlak analysis at the voxel level was performed with OLS to generate parametric images of  $K_i$ . VOIs were drawn over the tumour, the tumour's background (left lung) and the liver, as shown in figure 2, to compare between reconstructions and against the findings of the simulation study. Using these the contrast to noise ratio (CNR) was estimated according to

$$CNR = \frac{\theta_{tumour} - \theta_{bkg}}{\theta_{bkg} SD_{liver}}, \quad (9)$$

where  $SD_{VOI}$  is the spatial standard deviation of a VOI.

Similarly, CNR was calculated in a single noise realisation of the simulation study to enable direct comparison with the real data. In this case the eroded thalamus VOI was used as the target region and the white matter as the background for both contrast and noise estimation.

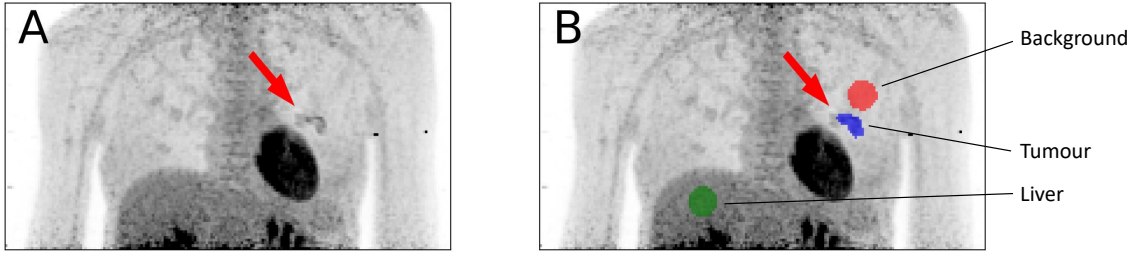


**Figure 2.** Real data MIP SUV image (A) and the drawn VOI (B).

### 3. Results

#### 3.1. Comparison between SB and DWB protocol data

The VOI and voxel based metrics comparing 3D and 4D Patlak reconstructions for the SB and DWB-1 protocols are shown in figure 3. For both metrics and VOIs the 3D reconstruction followed by post-reconstruction Patlak fitting using DWB data resulted in higher CoV values, compared to 3D reconstruction of SB data at matched bias. For the first few iterations the 3D reconstructions of both datasets resulted to similar bias values, while further iterations resulted to a wider range of bias values for the DWB data compared to SB data within 40 iterations.

The use of 4D Patlak reconstruction on DWB data produced results with lower CoV on both evaluated metrics and VOIs, compared to the 3D reconstruction of the same data at matched bias, and a shorter range of bias values within 40 iterations. For the VOI metrics, CoV values of the 4D Patlak reconstruction on both evaluated regions approach those of 3D reconstruction of SB data. Furthermore, the 4D Patlak reconstruction of DWB data resulted in eroded thalamus bias values that evolved towards a steady value of positive bias, at approximately iteration 12, after which further iterations resulted in small step changes towards lower bias. For the voxel metrics, similar behaviour is seen on early iterations of 4D Patlak reconstruction on DWB data for the CoV, with values approaching those of 3D reconstruction of SB data. But at further iterations the CoV for the 4D Patlak reconstruction in both VOIs surpasses values from 3D reconstruction on DWB data. On the eroded thalamus this was the case beyond iteration 24, while for the cortex from iteration 22 and beyond. These results show that there is a risk of increasing parametric image noise, greater than that of 3D reconstructions, when the 4D reconstruction is run at high iterations to achieve more favourable and stable mean VOI behaviour.

The use of 4D Patlak reconstruction with SB data showed similar effects on behaviour for CoV and bias on both metrics, compared to 3D reconstruction of SB data, and resulted in the lowest CoV values for these comparisons.

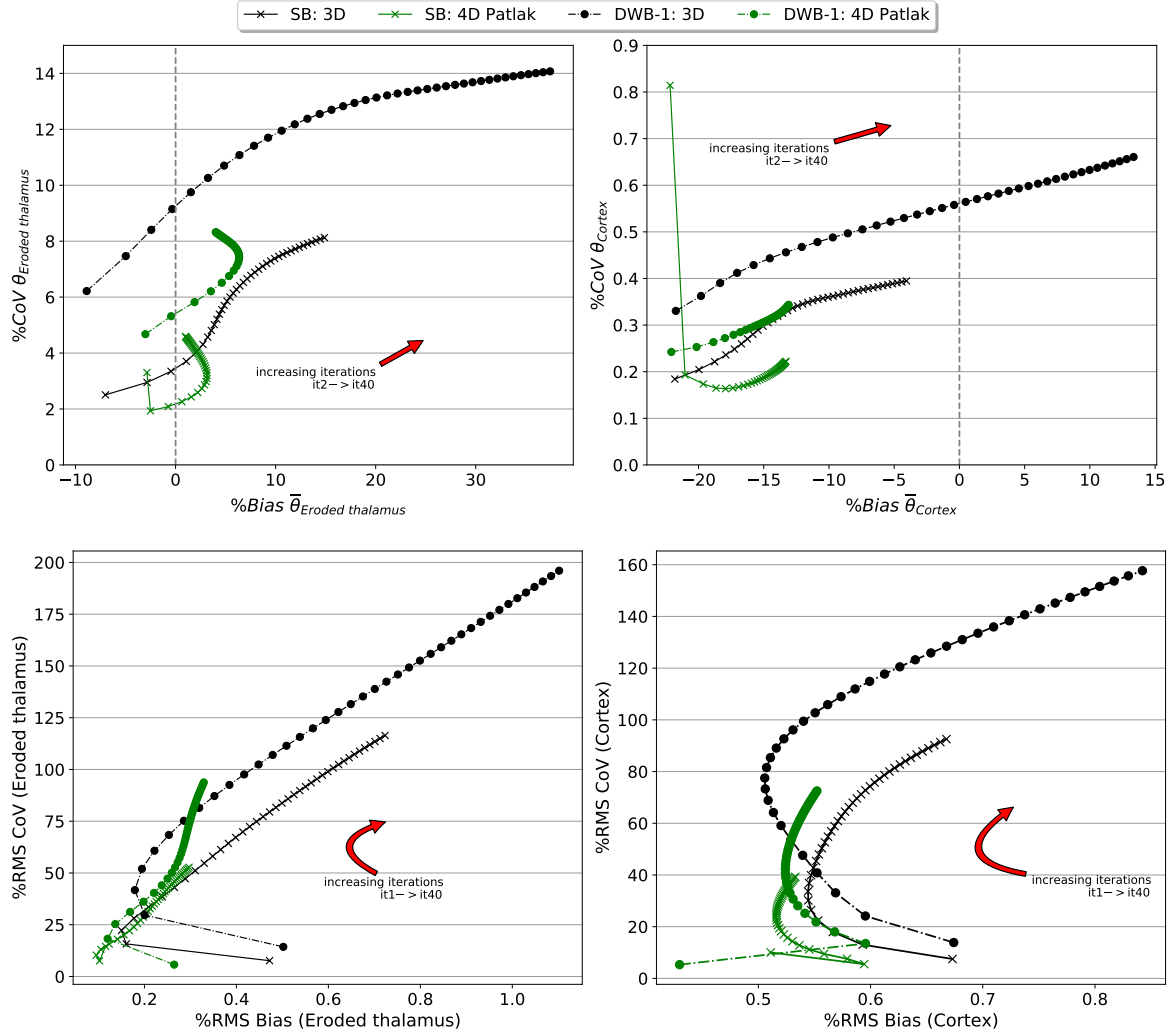


**Figure 3.** Simulation: Eroded thalamus (left) and Cortex (right) noise versus bias trade-off curves for 3D and 4D Patlak reconstructions. VOI based metrics (top row) and voxel-based metrics (bottom row).

### 3.2. Comparison between 4D Dynamic Reconstructions on DWB protocol data

The VOI and voxel based metrics are shown in figure 4 for comparison of 4D Patlak and 4D Spectral reconstructions of DWB data. On both metrics and for both regions the use of Spectral reconstruction with 6 basis functions provided the lowest CoV values at matched bias compared to other 4D reconstructions of DWB data and 3D reconstruction of SB data. However 4D Spectral reconstruction with 6 basis also provided the highest bias values in the eroded thalamus. On the cortex the difference on bias metrics was relatively small between all 4D reconstructions.

The 4D Spectral reconstruction with 9 and 17 basis functions resulted to similar bias and CoV values at both regions. Their use resulted in lower CoV compared to 4D Patlak reconstruction and 3D reconstruction of SB data, but higher compared to 4D Spectral using 6 basis. Nonetheless, at the eroded thalamus use of 9 and 17 basis provided

improved bias values at matched CoV when compared to the use of 6 basis, closer to bias values from 4D Patlak reconstruction.

When the 4D Spectral reconstructions were provided with the same data as the 4D Patlak reconstructions (4 frames with  $t > t_{ss}$ ) instead of all data (8 frames for DWB-1), it resulted in a noticeable increase of the CoV values, with very close noise versus bias trade-offs between 6 and 9 basis. Their trade-off curves got closer to the one of the 4D Patlak reconstruction, with lower bias values on both metrics but higher RMS CoV compared to the 4D Patlak reconstruction.

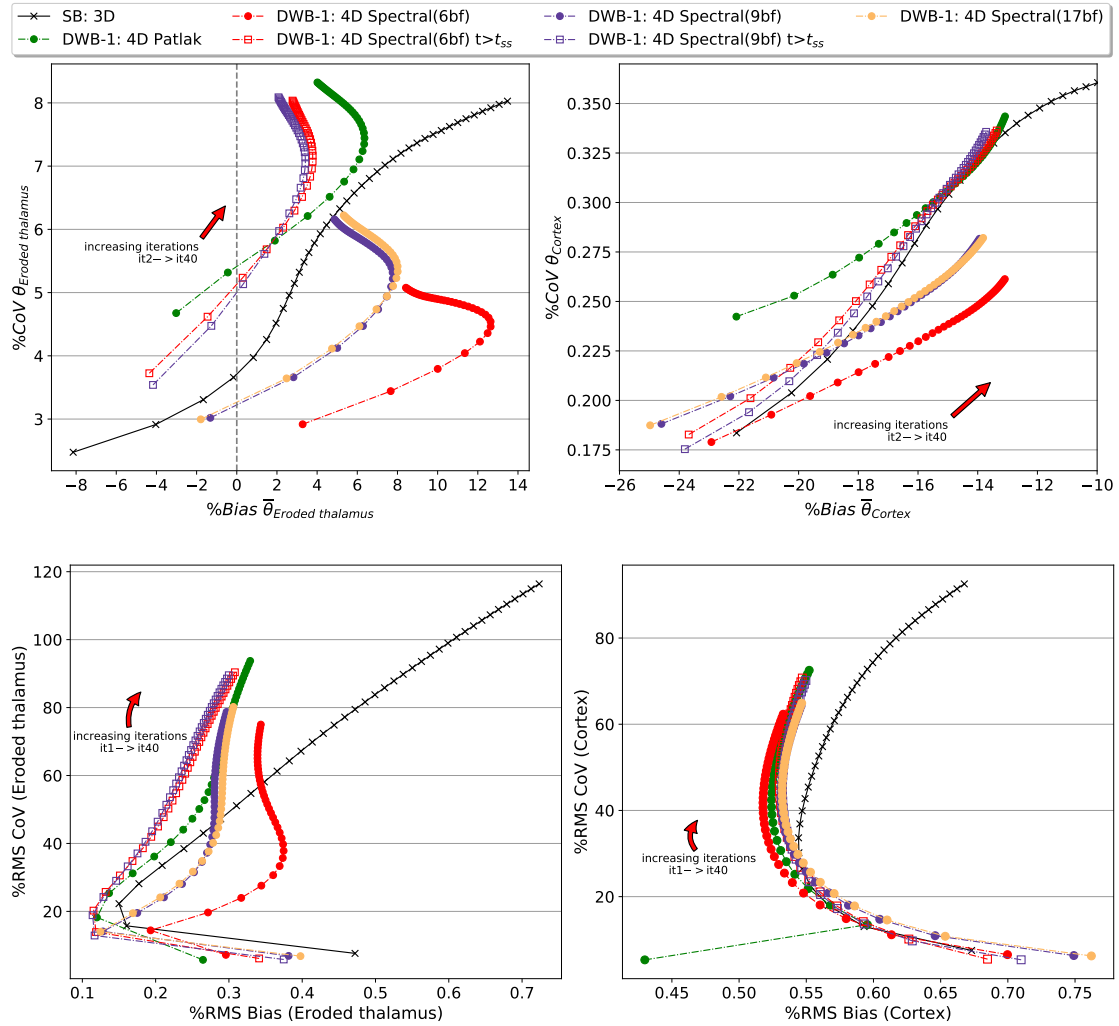


**Figure 4.** Simulation: Eroded thalamus (left) and Cortex (right) noise versus bias trade-off curves for 4D reconstructions of DWB-1 protocol data. VOI based metrics (top row) and voxel-based metrics (bottom row).

### 3.3. Comparing between nested optimizations in 4D reconstruction

Results of 4D Spectral and 4D Patlak reconstructions using MLEM and NNLS nested optimization are shown in figure 5. A clear difference in behaviour is seen going from

MLEM to NNLS from early iterations, with 4D reconstructions using nested NNLS optimization resulting in higher CoV values at matched bias compared to the respective 4D reconstruction using nested MLEM (with 20 nested sub-iterations). At the same time, NNLS nested optimization often resulted to a slight reduction in bias at matched CoV values. No difference was seen in convergence properties such as convergence speed between the two nested optimization options. Nevertheless the use of a single run of NNLS optimization in each nested loop, instead of 20 nested MLEM iterations, resulted in notable reduction of overall reconstruction times. The average reconstruction times using the two methods on a computer using a 16-core 2.20GHz processor and 96GB of RAM memory are shown in table 4.

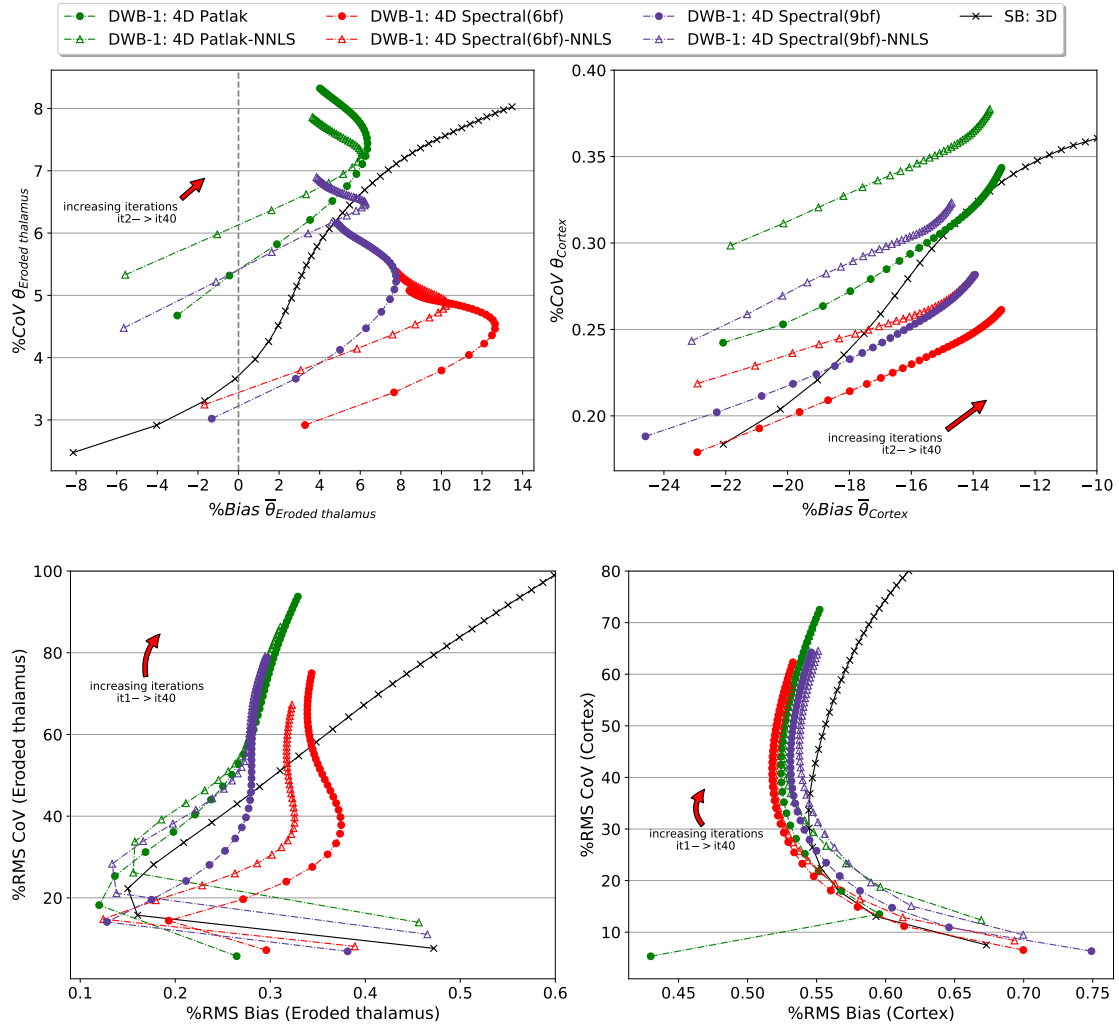


**Figure 5.** Simulation: Eroded thalamus (left) and Cortex (right) noise versus bias trade-off curves for 4D reconstructions, with MLEM and NNLS nested optimization. VOI based metrics (top row) and voxel-based metrics (bottom row).

**Table 4.** Average reconstruction times for 1 full iteration (28 subsets) over DWB-1 data using CASToR.

Reconstruction	nested MLEM (min)	nested NNLS (min)
4D Patlak	9.6	6.7
4D Spectral(6bf)	14.0	8.2
4D Spectral(9bf)	15.8	8.3
4D Spectral(17bf)	26.6	11.2

### 3.4. Comparison between DWB protocols

Comparison of 4D Patlak and 4D Spectral reconstructions between the three simulated DWB protocols is made in figure 6. For both VOI regions and 4D reconstructions, data from all three DWB protocols resulted in close bias values at matched iteration number, with a slight deviation in RMS bias towards late iterations. Differences in CoV at matched bias values are more profound in VOI metrics of the cortex region, where data from protocol DWB-2 resulted in the lowest CoV values and DWB-1 and DWB-3 data resulted to closer CoV values. This level of reduction in CoV was not seen on the eroded thalamus, neither on VOI or voxel based metrics. In the eroded thalamus the differences of DWB protocols on CoV at matched bias were smaller and their ordering was mixed between the two 4D reconstructions.

### 3.5. Comparison with real data

The comparison of reconstructions using a real FDG dataset, reprocessed and reconstructed with the SB and DWB-1 protocol framings, is made in figure 7. Results on the real data showed similar evolution of CNR with increasing iterations for all 4D and 3D reconstructions. The 4D Spectral reconstruction using 6 basis functions provided the highest CNR values throughout all iterations, followed by the 4D Spectral reconstruction using 9 basis functions and 4D Patlak. Overall, CNR of all 4D reconstructions of DWB data was higher than that of 3D reconstruction of SB data and 3D reconstruction of DWB data.

The tumour SD vs VOI average trade-off curves showed close behaviour between 4D reconstructions, resulting to SD values in the first 15 to 17 iterations of 4D reconstructions which were lower compared to 3D reconstruction of DWB data at matched tumour mean values. Compared to 3D reconstruction of SB data, all 4D reconstructions of DWB data resulted in higher SD values (for matched tumour mean values where comparison is possible). Parametric  $K_i$  images from 3D and 4D reconstructions at iterations with matched liver SD values of approximately  $4 \cdot 10^{-3} \text{ min}^{-1}$  are shown in figure 8.

For comparison against the simulation study, metrics of CNR and SD vs VOI average trade-off curves from a randomly chosen noise replicate of simulation DWB-1 are

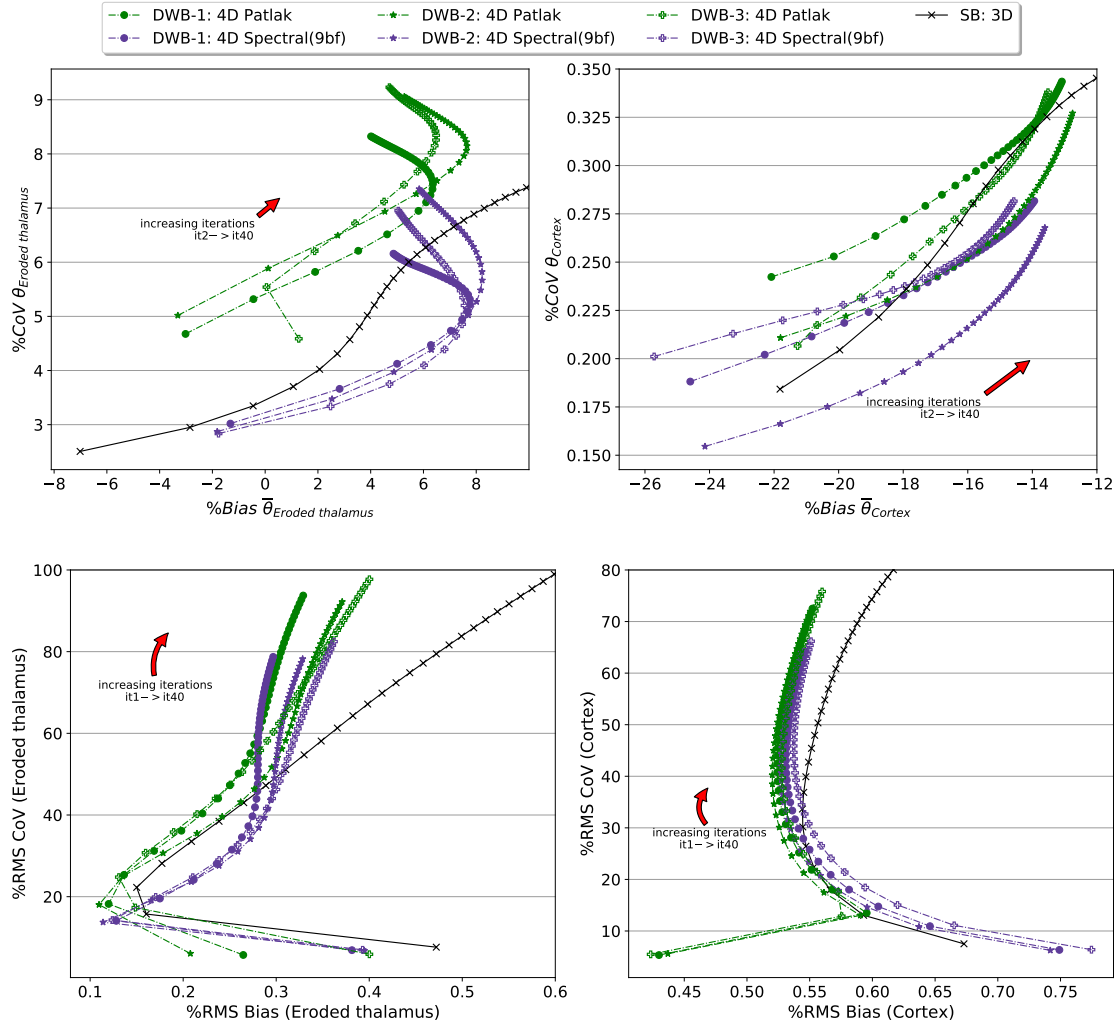


**Figure 6.** Simulation: Eroded thalamus (left) and Cortex (right) noise versus bias trade-off curves for 4D reconstructions of the simulated DWB protocol data. VOI based metrics (top row) and voxel-based metrics (bottom row).

shown in figure 9. Similarly to the real data, values of CNR are highest for 4D Spectral reconstruction using 6 basis functions, followed by 4D Spectral reconstruction using 9 basis functions. Contrary to the real data, 4D Patlak reconstruction provided lower CNR values compared to 4D Spectral reconstruction using 9 basis functions and closer to the values of 3D reconstruction from SB data. Furthermore, the initial evolution of CNR with increasing iterations was different from the real data, with maximum values attained at approximately 3 to 5 iterations for all reconstructions. On the real data maximum values were attained from the first iteration for all reconstructions. The difference in this direct comparison could potentially be attributed to the different nature of the VOIs used for CNR estimation and to different convergence behaviour due to use of TOF information in the reconstructions of the real data. Finally, the simulation data SD vs VOI average trade-off curves of the eroded thalamus showed separation of 4D



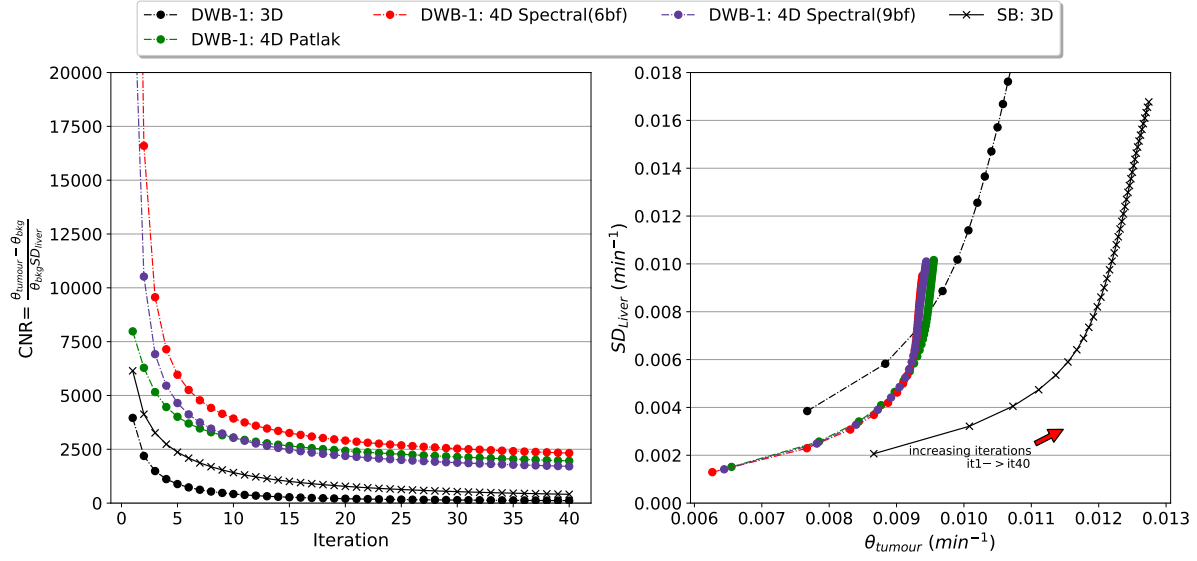


**Figure 7.** Real Data: Contrast to Noise ratio (left) and liver SD vs. VOI mean of the tumour (right) for 3D and 4D reconstructions.

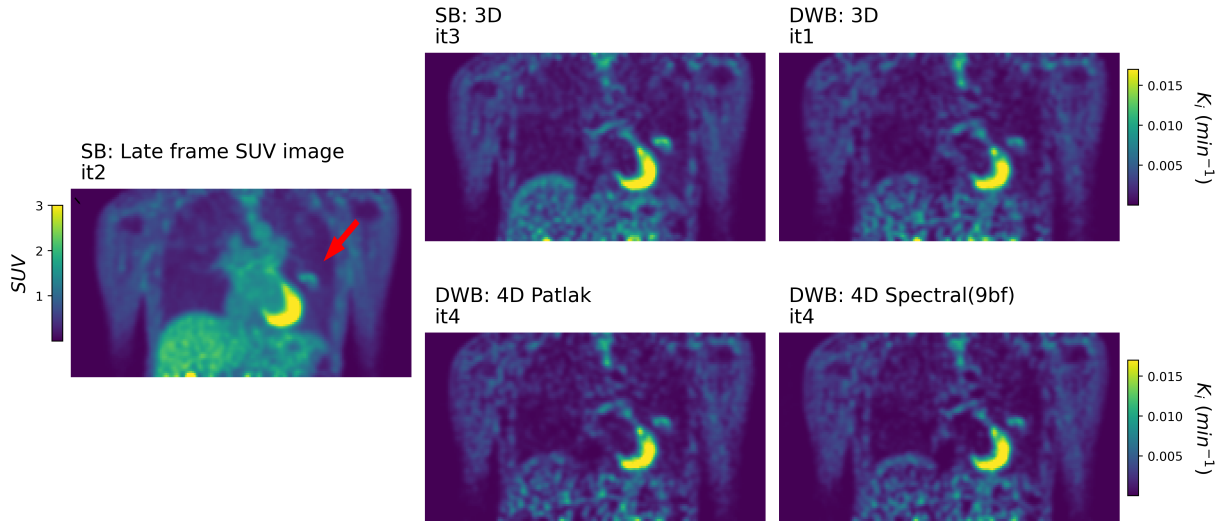


**Figure 8.** Real Data: Parametric  $K_i$  images (with 5mm Gaussian Filtering) from SB and DWB replay datasets from 3D and 4D reconstructions at matched SD values over the liver.

reconstructions, with 4D Spectral reconstructions providing lower SD values compared to 3D and 4D Patlak reconstruction of DWB data, but at higher bias values as shown previously in the analysis of simulation results. Parametric  $K_i$  images of 3D and 4D reconstructions at matched RMS CoV values, of approximately 32% as measured at the eroded thalamus VOI, are shown in figure 10 for a single noise replicate along with images of mean bias over noise replicates. The single replicate images show that structures of the thalamus seen in 3D reconstruction of SB data are better resolved in DWB when using the 4D Spectral reconstruction. The images of bias show similar behaviour in the

thalamus over reconstructions and demonstrate the partial volume effects at the cortex region.

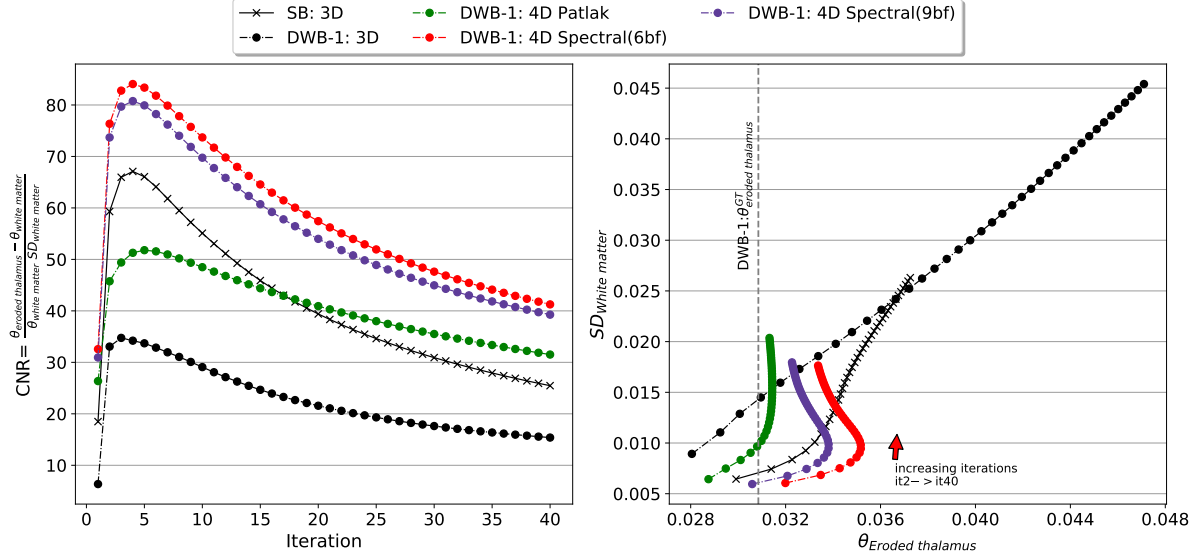


**Figure 9.** Simulation single noise realisation of DWB-1 data: Contrast to Noise ratio (left) and white matter SD vs. eroded thalamus  $K_i$  mean for 3D and 4D reconstructions.

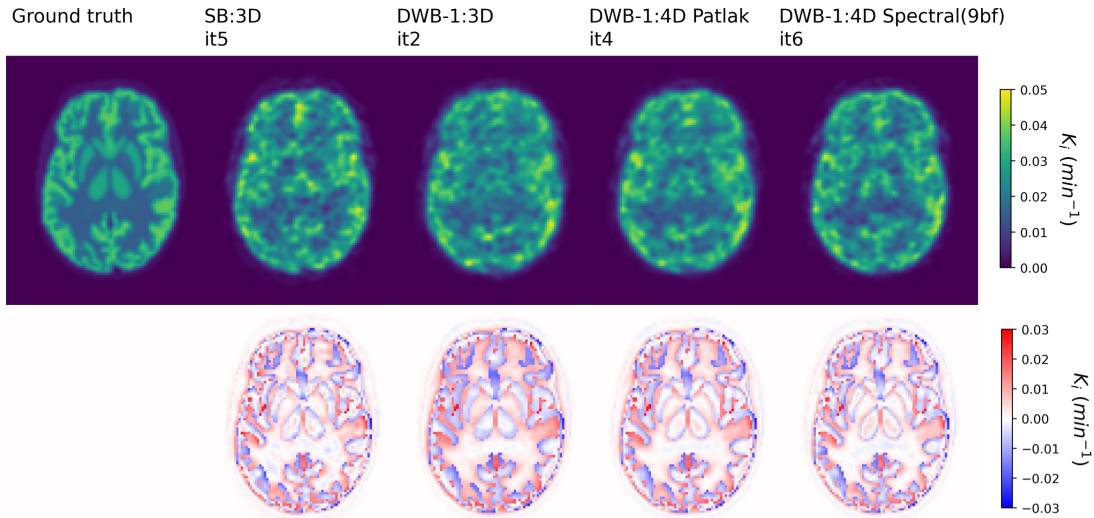


**Figure 10.** Single slice through parametric  $K_i$  images of one noise replicate (with 3mm Gaussian Filtering) (top) and their corresponding Bias images (over noise replicates) (bottom) from SB and DWB data 3D and 4D reconstructions at matched RMS CoV in the eroded thalamus.

#### 4. Discussion

Our simulation study shows that the dynamic reconstruction of DWB FDG data resulted in substantial reduction of Patlak  $K_i$  image noise and more favourable convergence behaviour, compared to 3D reconstruction based parametric imaging. These results, limited to a single level of noise, are in agreement with the findings of (Karakatsanis, Casey, Lodge, Rahmim & Zaidi 2016). Moreover, we directly compared against a SB dynamic protocol, processed with 3D reconstruction, and showed that comparable values of parametric image noise and bias can be achieved with DWB protocols by the use of a dynamic reconstruction. The choice of the iteration number to terminate a 4D reconstruction algorithm is not evident. For a VOI-based analysis, the convergence of the mean  $K_i$  value in the cortex or in the eroded thalamus was not seen in the range of the 40 evaluated OSEM iterations, in particular for a 3D reconstruction. This behaviour was also observed for a 4D reconstruction algorithm, but to a lesser extent. A high number of iterations of 4D reconstruction algorithms provided more stable VOI mean values, but at risk of resulting to higher parametric image noise than that of a 3D reconstructions on the same DWB data. The results obtained with one real dataset showed similar behaviour with mean VOI values continuing to slightly increase even after 40 OSEM iterations and with 4D reconstruction parametric image noise surpassing that of 3D reconstruction at late iterations. This example illustrates that the relative aspects of 4D to 3D comparisons with simulated data for the tested DWB and SB protocols have the capacity to translate to studies with different levels of noise. A limitation in this comparison with real data is that the use of TOF in real data can alter the convergence behaviour which could potentially explain the differences seen in the evolution of CNR with iteration. Nonetheless, the ranking of the reconstructions with respect to the result CNR was similar between simulation and the real study. Overall, the risks of excessive parametric image noise and under-converged  $K_i$  values will be lesser for 4D based reconstruction methods than for a 3D reconstruction, which demonstrated considerably more instability with increasing iterations. To ensure convergence of the  $K_i$  values while suppressing the increase of parametric image noise, further regularisation techniques can be used with methods such as 4D MAP reconstruction (Reader & Verhaeghe 2014, Wang et al. 2008) or kernel 4D dynamic reconstruction (Novosad & Reader 2016, Gong et al. 2018).

Our nested optimization tests using NNLS instead of multiple MLEM sub-iterations did not provide any differences in the acceleration of the convergence and showed comparable behaviour to a previous study on the use of NNLS with the spectral model (Matthews et al. 2010). NNLS did provide computing acceleration by a factor of around two for our data sets, but resulted in an increase of the parametric image noise compared to MLEM sub-iterations for similar bias characteristics. Equivalent or higher acceleration could be potentially achieved if the nested MLEM optimization was conducted in graphical processing units (GPU) instead of the CPUs.

In this work, we evaluated the use of an indirect dynamic reconstruction

method based on a generic 4D Spectral reconstruction algorithm followed by a post-reconstruction Patlak model fitting. The genericity of the spectral model allows for flexibility in modeling dynamic processes that do not necessarily fall under the idealised behaviour of the kinetic model of interest. In this simulation study, we were limited to irreversible FDG kinetics that can be sufficiently described by the Patlak model. In this case, 4D Spectral reconstruction making use of the full dynamic data outperformed the direct Patlak reconstruction in terms of parametric image noise, while maintaining similar bias behaviour. The benefit of the 4D spectral reconstruction was less obvious when fewer frames were used in reconstructions using  $t > t_{ss}$ , indicating that its favourable behaviour was mostly due to the use of more temporal frames than the Patlak reconstruction. In real FDG studies, it can be desirable to account for reversible FDG kinetics and reduce the bias of the estimated macro-parameters arising from poorly modelled kinetics. The spectral model can allow for more complex compartmental modeling with no strong prior knowledge or enforcement of a specific model. As such it can account for more complex kinetic behaviours, including reversibility of tracer, in the reconstruction process and allow for post-reconstruction exploratory modeling to identify the best model to describe and present the data. Moreover for DWB studies where not all body regions and organs will necessarily be adequately described by a single dynamic model of interest, the proposed indirect method can allow for the assignment of different kinetic models in different regions of the body to ensure appropriate representation of the dynamic tracer behaviour. Depending on the availability of early frame data, the fitted spectral model can be used to directly estimate  $K_1$  (Meikle et al. 1998, Matthews et al. 2010), while post-reconstruction micro-parameter estimation could be performed for potential uses in clinical applications (Novosad & Reader 2016, Zaker et al. 2020) and indirectly take advantage of the 4D reconstruction temporal regularisation. An important parameter to configure for the spectral model is the number of basis function. Contrary to post-reconstruction spectral analysis where hundreds of basis functions are used to finely sample the space of kinetic exchange rates, a smaller number of basis is desirable in reconstruction to favour reduced image noise. In some cases of our findings the lowest number of basis functions used (6 basis) resulted in higher bias values which indicates less than adequate modeling of the underlying kinetics, compared to reconstructions with more basis functions and to 4D Patlak reconstruction. However this was not the case when fewer frames were used in reconstructions using  $t > t_{ss}$  data. These findings indicate that the selection of number of basis functions is important not only for controlling the produced image noise but also for controlling bias by adequately modeling the kinetics behaviour in reconstruction. For the higher numbers of basis functions, with 9 and 17, almost identical behaviour was seen on the DWB-1 dataset (of 8 frames). Overall on the choice of number of basis functions, results indicate a greater risk in image bias when using a too small number of basis functions, and a lesser risk in image noise when using more basis functions than strictly needed to properly model the underlying kinetics. In any case the number of basis needs to be tuned for every DWB protocol, depending on the number of frames within the dataset

and the range of underlying kinetics as well as the level of noise in the PET data.

In this study, the investigation between S&S and CBM DWB protocols was limited to aspects of sampling frequency and uniformity within the total examination time. Our results showed small differences in parametric image bias but noticeable reduction in parametric image noise when utilising CBM acquisition with uniform sampling. Overall differences were inline with previous findings of comparison S&S and CBM on a real data study using different metrics (Karakatsanis, Garibotto, Rager & Zaidi 2016). A limitation in our study is that we have considered a single axial location and hence we cannot generalise the results of the simulation study for the performance of the assumed DWB protocols over their effective FOV. Furthermore beyond the aspects of reduced acquisition delays and higher sampling frequency, CBM acquisition has other desirable properties for DWB acquisitions as outlined previously (Karakatsanis, Garibotto, Rager & Zaidi 2016). The most important aspect is the result uniform axial sensitivity profile at any choice of acquisition speed. That can be of importance in DWB parametric imaging where multiple regions of interest are expected in the effective FOV. In our study we have not considered this aspect for the CBM protocols and we did not examine regions in the overlap range of the S&S protocol. But the observed improvements related to reduced delays in acquisition coupled with uniformity of axial sensitivity favour the choice of CBM over S&S protocols. We investigated further potential reductions in system delays by allowing for non-uniform axial sampling using bi-directional CBM. In that case we did not see the same effects as in the transition from S&S to CBM. But our results on bi-directional CBM are limited to the specific framing of the evaluated protocol design which offered more total frames but resulted in less total counts compared to the other protocols. Additional tests are required on the exploitation of the flexibility offered by bi-directional CBM to assess other potential benefits against uni-directional CBM.

## 5. Conclusion

4D dynamic reconstruction is necessary in DWB parametric imaging to achieve accurate and stable quantification. For FDG Patlak  $K_i$  parametric imaging we have shown results of direct Patlak dynamic reconstruction with noise and bias values that were comparable to 3D reconstruction based parametric imaging from single bed dynamic studies. In this work we proposed the use of an indirect method for DWB parametric imaging, based on the spectral analysis model. This more flexible approach allows for complex kinetic modelling to be used during reconstruction for temporal regularisation, with minimal assumptions on the underlying kinetics. In Patlak  $K_i$  parametric imaging this method outperformed the direct Patlak approach, by making use of all the acquired data for temporal regularisation from which post-reconstruction parametric imaging benefitted by further reduction of noise compared to the Patlak approach. Furthermore, the spectral model approach can be used for more complex post-reconstruction modelling, for example in parametric imaging of FDG micro-parameters. Finally, we investigated

the impact of various acquisition modes (for CBM and S&S) resulting in different temporal sampling of the data. Benefits of reduced delays and increased acquisition statistics were partially seen in reduced parametric image noise for the CBM protocol with uni-directional axial sampling. By contrast CBM using bi-directional motion resulted to parametric image noise levels that were similar to the S&S protocol. Further investigation is required to assess the potential benefits from bi-directional CBM against uni-directional CBM and effects of non-uniform sampling over the entire FOV of the DWB protocols.

Overall, use of 4D dynamic reconstruction for DWB parametric imaging offers desirable properties that enables the transition from single bed dynamic studies and common 3D reconstruction parametric imaging practices without loss of image quality and with additional benefits for accuracy of parametric images. Potential applications of DWB parametric imaging are expected to rely on quantification of images and so there should be no compromise between parametric image accuracy and image noise. Our results showed that 4D reconstruction need to be sufficiently iterated to ensure accurate quantification, with potential for improvement in maintaining low parametric image noise by use of additional regularisation methods.

## Acknowledgments

This project has received funding from the European Union’s Horizon 2020 research and innovation programme under the Marie Skłodowska-Curie grant agreement No 764458. This work was performed on a platform of France Life Imaging network partly funded by the grant ANR-11-INBS-0006. The authors would like to thank Dr. Florent Besson for providing the FDG Dynamic dataset and the delienation of the tumour volume.

## References

- Boellaard, R. (2011). Need for standardization of 18F-FDG PET/CT for treatment response assessments, *Journal of Nuclear Medicine* **52**(Suppl. 2): 93–100.
- Carson, R. E. & Lange, K. (1985). Comment: The EM parametric image reconstruction algorithm, *Journal of the American Statistical Association* **80**(389): 20–22.
- Cherry, S. R., Jones, T., Karp, J. S., Qi, J., Moses, W. W. & Badawi, R. D. (2018). Total-Body PET: Maximizing Sensitivity to Create New Opportunities for Clinical Research and Patient Care, *Journal of Nuclear Medicine* **59**(1): 3–12.
- Cunningham, V. J. & Jones, T. (1993). Spectral Analysis of Dynamic PET Studies, *Journal of Cerebral Blood Flow & Metabolism* **13**(1): 15–23.
- Dias, A., Pedersen, M., Danielsen, H., Munk, O. & Gormsen, L. (2020). Improved lesion detection in Whole-Body Parametric 18F-FDG PET/CT vs. Static 18F-FDG PET/CT, *Journal of Nuclear Medicine* **61**(supplement 1): 97–97.
- Dimitrakopoulou-Strauss, A., Pan, L. & Sachpekidis, C. (2021). Kinetic modeling and parametric imaging with dynamic PET for oncological applications: general considerations, current clinical applications, and future perspectives, *European Journal of Nuclear Medicine and Molecular Imaging* **48**(1): 21–39.
- Fahrni, G., Karakatsanis, N. A., Di Domenicantonio, G., Garibotto, V. & Zaidi, H. (2019). Does

- whole-body Patlak 18F-FDG PET imaging improve lesion detectability in clinical oncology?, *European Radiology* **29**(9): 4812–4821.
- Gong, K., Cheng-Liao, J., Wang, G., Chen, K. T., Catana, C. & Qi, J. (2018). Direct Patlak Reconstruction from Dynamic PET Data Using the Kernel Method with MRI Information Based on Structural Similarity, *IEEE Transactions on Medical Imaging* **37**(4): 955–965.
- Grant, A. M., Deller, T. W., Khalighi, M. M., Maramraju, S. H., Delso, G. & Levin, C. S. (2016). NEMA NU 2-2012 performance studies for the SiPM-based ToF-PET component of the GE SIGNA PET/MR system, *Medical Physics* **43**(5): 2334–2343.
- Gunn, R. N., Gunn, S. R., Turkheimer, F. E., Aston, J. A. D. & Cunningham, V. J. (2002). Positron Emission Tomography Compartmental Models: A Basis Pursuit Strategy for Kinetic Modeling, *Journal of Cerebral Blood Flow & Metabolism* **22**(12): 1425–1439.
- Hu, J., Panin, V., Kehren, F. & Casey, M. (2014). Gated reconstruction for PET scan with continuous bed motion, *2014 IEEE Nuclear Science Symposium and Medical Imaging Conference (NSS/MIC)*, IEEE, pp. 1–3.
- Hu, J., Panin, V., Smith, A. M., Spottiswoode, B., Shah, V., CA von Gall, C., Baker, M., Howe, W., Kehren, F., Casey, M. & Bendriem, B. (2020). Design and Implementation of Automated Clinical Whole Body Parametric PET With Continuous Bed Motion, *IEEE Transactions on Radiation and Plasma Medical Sciences* **4**(6): 696–707.
- Kamasak, M., Bouman, C., Morris, E. & Sauer, K. (2005). Direct reconstruction of kinetic parameter images from dynamic PET data, *IEEE Transactions on Medical Imaging* **24**(5): 636–650.
- Karakatsanis, N. A., Casey, M. E., Lodge, M. A., Rahmim, A. & Zaidi, H. (2016). Whole-body direct 4D parametric PET imaging employing nested generalized Patlak expectation-maximization reconstruction, *Physics in Medicine and Biology* **61**(15): 5456–5485.
- Karakatsanis, N. A., Garibotto, V., Rager, O. & Zaidi, H. (2016). Continuous bed motion Vs. step-and-shoot acquisition on clinical whole-body dynamic and parametric PET imaging, *2015 IEEE Nuclear Science Symposium and Medical Imaging Conference, NSS/MIC 2015*, Institute of Electrical and Electronics Engineers Inc.
- Karakatsanis, N. A., Lodge, M. A., Tahari, A. K., Zhou, Y., Wahl, R. L. & Rahmim, A. (2013). Dynamic whole-body PET parametric imaging: I. Concept, acquisition protocol optimization and clinical application, *Physics in Medicine and Biology* **58**(20): 7391–7418.
- Karakatsanis, N. A., Lodge, M. A., Zhou, Y., Mhlanga, J., Chaudhry, M. A., Tahari, A. K., Segars, W. P., Wahl, R. L. & Rahmim, A. (2011). Dynamic Multi-Bed FDG PET Imaging: Feasibility and Optimization, *2011 IEEE Nuclear Science Symposium and Medical Imaging Conference (NSS/MIC)*, pp. 3863–3870.
- Karp, J. S., Viswanath, V., Geagan, M. J., Muehllehner, G., Pantel, A. R., Parma, M. J., Perkins, A. E., Schmall, J. P., Werner, M. E. & Daube-Witherspoon, M. E. (2020). PennPET explorer: Design and preliminary performance of a whole-body imager, *Journal of Nuclear Medicine* **61**(1): 136–143.
- Lammertsma, A. A. (2017). Forward to the past: The case for quantitative PET imaging, *Journal of Nuclear Medicine* **58**(7): 1019–1024.
- Lawson, C. L. & Hanson, R. J. (1995). *Solving Least Squares Problems*, Society for Industrial and Applied Mathematics.
- Matthews, J., Ashburner, J., Bailey, D., Harte, R., Price, P. & Jones, T. (1995). Direct calculation of parametric images from raw pet data using maximum likelihood iterative reconstruction, *IEEE Nuclear Science Symposium & Medical Imaging Conference* **2**: 1311–1315.
- Matthews, J. C., Angelis, G. I., Kotasidis, F. A., Markiewicz, P. J. & Reader, A. J. (2010). Direct reconstruction of parametric images using any spatiotemporal 4D image based model and maximum likelihood expectation maximisation, *IEEE Nuclear Science Symposium Conference Record* (4): 2435–2441.
- Meikle, S. R., Matthews, J. C., Cunningham, V. J., Bailey, D. L., Livieratos, L., Jones, T. & Price,

- P. (1998). Parametric image reconstruction using spectral analysis of PET projection data, Physics in Medicine and Biology **43**(3): 651–666.
- Meikle, S. R., Sossi, V., Roncali, E., Cherry, S. R., Banati, R., Mankoff, D., Jones, T., James, M., Sutcliffe, J., Ouyang, J., Petibon, Y., Ma, C., El Fakhri, G., Surti, S., Karp, J. S., Badawi, R. D., Yamaya, T., Akamatsu, G., Schramm, G., Rezaei, A., Nuyts, J., Fulton, R., Kyme, A., Lois, C., Sari, H., Price, J., Boellaard, R., Jeraaj, R., Bailey, D. L., Eslick, E., Willowson, K. P. & Dutta, J. (2021). Quantitative PET in the 2020s: A roadmap, Physics in Medicine and Biology **66**(6).
- Merlin, T., Stute, S., Benoit, D., Bert, J., Carlier, T., Comtat, C., Filipovic, M., Lamare, F. & Visvikis, D. (2018). CASToR: a generic data organization and processing code framework for multi-modal and multi-dimensional tomographic reconstruction, Physics in Medicine & Biology **63**(18): 185005.
- Novosad, P. & Reader, A. J. (2016). MR-guided dynamic PET reconstruction with the kernel method and spectral temporal basis functions, Physics in Medicine and Biology **61**(12): 4624–4645.
- Panin, V. Y., Smith, a. M., Hu, J., Kehren, F. & Casey, M. E. (2014). Continuous bed motion on clinical scanner: design, data correction, and reconstruction., Physics in medicine and biology **59**(20): 6153–74.
- Rahmim, A., Lodge, M. A., Karakatsanis, N. A., Panin, V. Y., Zhou, Y., McMillan, A., Cho, S., Zaidi, H., Casey, M. E. & Wahl, R. L. (2019). Dynamic whole-body PET imaging: principles, potentials and applications, European Journal of Nuclear Medicine and Molecular Imaging **46**(2): 501–518.
- Reader, A. J., Matthews, J. C., Sureau, F. C., Comtat, C., Trébossen, R. & Buvat, I. (2007). Fully 4D image reconstruction by estimation of an input function and spectral coefficients, IEEE Nuclear Science Symposium Conference Record **5**(1): 3260–3267.
- Reader, A. J. & Verhaeghe, J. (2014). 4D image reconstruction for emission tomography, Physics in Medicine and Biology **59**(22): R371–R418.
- Schubert, S. F., Pajevic, S. & Carson, R. E. (1996). Whole body PET using overlapped 3D acquisition and weighted image summation, IEEE Nuclear Science Symposium & Medical Imaging Conference **2**: 1285–1289.
- Siegel, S., Mehmet, A., Bal, H., Bendriem, B., Bharkhada, D., Cabello, J., Eriksson, L., Panin, V., Rothfuss, H. & Conti, M. (2020). Preliminary Performance of a Prototype, One Meter Long PET Tomograph, 2020 IEEE Nuclear Science Symposium and Medical Imaging Conference (NSS/MIC), pp. 1–2.
- Stute, S., Tauber, C., Leroy, C., Bottlaender, M., Brulon, V. & Comtat, C. (2015). Analytical simulations of dynamic PET scans with realistic count rates properties, 2015 IEEE Nuclear Science Symposium and Medical Imaging Conference (NSS/MIC), pp. 1–3.
- Subramaniam, R. M. (2017). Precision Medicine & PET/CT: Challenges and Implementation Rathan, PET Clinics **12**(1): 1–5.
- Vandenberghe, S., Moskal, P. & Karp, J. S. (2020). State of the art in total body PET, EJNMMI Physics **7**(1).
- Wang, G., Fu, L. & Qi, J. (2008). Maximum a posteriori reconstruction of the Patlak parametric image from sinograms in dynamic PET, Physics in Medicine and Biology **53**(3): 593–604.
- Wang, G. & Qi, J. (2010). Acceleration of the direct reconstruction of linear parametric images using nested algorithms, Physics in Medicine and Biology **55**(5): 1505–1517.
- Zaker, N., Kotasidis, F., Garibotto, V. & Zaidi, H. (2020). Assessment of Lesion Detectability in Dynamic Whole-Body PET Imaging Using Compartmental and Patlak Parametric Mapping, Clinical Nuclear Medicine **45**(5): E221–E231.
- Zubal, I. G., Harrell, C. R., Smith, E. O., Rattner, Z., Gindi, G. & Hoffer, P. B. (1994). Computerized three-dimensional segmented human anatomy, Medical Physics **21**(2): 299–302.